HiSST: 3rd International Conference on
High-Speed Vehicle Science Technology
14 -19 April 2024, Busan, Korea

A Boundary Layer Analysis on the HEXAFLY-INT Experimental Flight Test Vehicle

Frederik Jacobs [1], Johan Steelant [2]

Abstract

As the development of hypersonic flight vehicles is rapidly accelerating, engineers are facing different challenges throughout the design cycle. One of these challenges is the avoidance of hot spots and induced boundary layer transition. Different correlations exist that could be used by designers, but they require specific parameters like boundary layer thickness and edge properties, streamline length, stagnation lines etc… which are not directly provided by a CFD solution. To extract these specific parameters, the Boundary Layer Identification and Transition Zone Detection (BLITZ) code was developed in a previous phase. To further extend the BLITZ tool capabilities and improve its accuracy, a blending methodology between the laminar and turbulent field solution is developed based on an intermittency factor. Together with the implementation of a standalone monitoring property calculation algorithm, it is now possible to make an improved estimate of the total heat load into the vehicle as well as the aerodynamic forces exerted on it considering the evolution of the transitional flow regime. Additionally, improvements on the boundary layer edge detection are presented. A comparison has been made between purely laminar, purely turbulent and transitional flow along the flight trajectory of the HEXAFLY-INT Experimental Flight Test Vehicle regarding boundary layer state, integrated heat load and aerodynamic force. Finally, a first analysis of the effect of the boundary layer state on the weight of the vehicle is provided.

Keywords: *HEXAFLY-INT, Boundary layer transition, Laminar-turbulent blending, Heat load, Aerodynamic Forces*

Nomenclature

Abbreviations
AoA – Angle of Attack
BLITZ – Boundary Layer Identification and Transition Zone Detection Code
CFD – Computational Fluid Dynamics
DLR – Deutsches Zentrum für Luft- und Raumfahrt (German Aerospace Center)
EFTV – Experimental Flight Test Vehicle
GTOW – Gross Take-Off Weight
HXI – HEXAFLY-International
TPS – Thermal Protection System

Latin
A – Area
D – Drag
I_{sp} – Specific Impulse
k – Thermal conductivity
l – Length
L – Lift
Ma – Mach number
p – Pressure
q – Heat flux
Q – Integrated heat load
R – Range
Re – Reynolds number
T – Temperature
Tu – Turbulence intensity
u – Velocity
V – Velocity
W – Weight
x – Streamwise direction
y – Wall normal direction

[1] *European Space Agency (ESTEC), Keplerlaan 1, 2201AZ Noordwijk, The Netherlands, Frederik.Jacobs@esa.int*
[2] *European Space Agency (ESTEC), Keplerlaan 1, 2201AZ Noordwijk, The Netherlands, Johan.Steelant@esa.int*

Greek
α – Relaxation factor
α_n – Coefficient for derivative criterion
β – Coefficient for derivative criterion
γ – Intermittency
ϵ – Emissivity
θ – Momentum thickness
μ – Viscosity
σ – Shear stress
σ – Stefan-Boltzmann constant
ϕ – Arbitrary flow variable

Subscripts
e – Value at the boundary layer edge
la – Landing
lam – Laminar
new – New simulation value
old – Previous simulation value
to – Take-Off
$turb$ – Turbulent
tr – Transition
$trans$ – Transitional
w – Value at the wall
∞ – Value at the farfield
0 – Reference value

1. Introduction

The white paper stemming from the outcome of the workshop on High-Speed Boundary Layer Transition at the HiSST conference in 2023 [1] identified critical needs during the design phase of high-speed flight vehicles. A correct evaluation of transition onset and extent, along with the minimum requirements related to protuberances were highlighted as one of the critical needs to be developed.

One of these needs is the avoidance of hot spots and induced boundary layer transition. Though different correlations exist that could be used by designers, they cannot be applied directly to computational fluid dynamics (CFD) simulations as they require specific parameters such as Reynolds numbers based upon displacement or momentum thicknesses and boundary layer edge properties, streamline length etc… which are not directly provided as a CFD outcome. To bridge this gap the Boundary Layer Identification and Transition Zone Detection (BLITZ) code was developed [2], [3], [4]. It calculates, starting from an existing CFD solution, all required boundary layer parameters and applies the requested correlations.

In [2], a first validation has been shown as well as a first application on the Ariane 5 fairing. To further extend the applicability of the tool, a sharp-edged body is analysed. For that reason, the experimental flight test vehicle (EFTV) of the HEXAFLY-INT (HXI) mission was selected [5]. The HXI project aims to develop an innovative high-speed glider, which will be tested during a free-flight test [6], [7] using the EFTV. To further assess the influence of the flowfield on the transition location, a monitoring algorithm is developed which can calculate autonomously local and integrated properties like drag and heat from the simulation file. Previously, these properties were extracted pointwise manually for transition analysis [7] which was cumbersome and spatially and temporally limited along the trajectory and vehicle's surface. The present tool assures the complete surface is entirely assessed for all calculated trajectory points.

Additionally, an algorithm is created which linearly blends the laminar and turbulent field solution such that an iterative approach can be applied to assess the location of transition as well as the aerodynamic and thermal loads when the flow is transitional. However, this linear blending, originally proposed by Dhawan and Narsimha [8] is only a zero-order approach towards a representation of a transitional flow regime whereas Steelant et al. [9], [10], [11], [12] demonstrated mathematically that conditionally averaging is needed to account for the actual interaction of the turbulent spot embedded within the laminar flow. Only in this latter approach, the blending is correctly representing the actual averaged properties. However, in the context of a first quick assessment, linear blending is justified to provide a first estimate of the transitional flow properties and the related integrated loads. Additional improvements on the boundary layer edge detection algorithm are discussed as well.

This paper presents an analysis of the evolution of the boundary layer transition onset along the trajectory of the EFTV. Both the aerodynamic and heat load are shown and compared for a fully laminar, a fully turbulent and a blended transitional flow. These properties offer an input to the sizing of the thermal protection system, the propulsion system and the trajectory calculation. This is illustrated by a calculation of the reduction in vehicle weight if boundary layer transition would be considered during the design phase of the vehicle.

2. BLITZ development

To further enhance the capabilities of the BLITZ tool, several improvements are realized. This paper discusses the development of an independent integrated property calculation methodology, the blending of laminar and turbulent simulations based on the intermittency and an improved boundary layer edge detection algorithm. Other improvements were made to enhance the accuracy of the streamline tracing and the related streamwise pressure gradient calculation, important to simulate the transition length. The latter two are not further discussed within this work.

2.1. Monitoring properties

To assess the surface integrated properties, a monitoring algorithm has been written which allows to calculate the viscous force, pressure force and heat flux for all simulations. These are analysed using the default equations for the viscous tension at the surface and applying the force in the near wall velocity direction.

$$\sigma_w = \mu_w \left(\frac{du}{dy}\right)_w \quad \text{Eq. 1}$$

For the heat flux a similar approach is using the thermal conductivity of air k:

$$q_w = k_w \left(\frac{dT}{dy}\right)_w \quad \text{Eq. 2}$$

If the viscosity μ or the thermal conductivity k are not present in the solution output file, the Sutherland formulation is applied, i.e.,

$$\frac{\mu}{\mu_0} = \left(\frac{T}{T_0}\right)^{\frac{3}{2}} \frac{T_0 + S}{T + S} \quad \text{Eq. 3}$$

$$\frac{k}{k_0} = \left(\frac{T}{T_0}\right)^{\frac{3}{2}} \frac{T_0 + S}{T + S} \quad \text{Eq. 4}$$

for which the coefficients are shown in Table 1 for air.

Table 1. Sutherland coefficients for air

$\boldsymbol{\mu_0}$	$\boldsymbol{k_0}$	$\boldsymbol{S}$	$\boldsymbol{T_0}$
$1.716 * 10^{-5} \frac{N.s}{m^2}$	$2.394 * 10^{-2} \frac{W}{m.K}$	$110.4K$	$273K$

Alternatively, the heat flux could also be calculated using the radiative heat, i.e.,

$$q_w = \sigma\epsilon(T^4 - T_\infty^4) \quad \text{Eq. 5}$$

in which ϵ is the surface emissivity and σ is the Stefan-Boltzmann constant.

As the wall is modelled by different elements, the average tension and heat flux value as well as the average of the flow directions of the corner nodes is taken to calculate the total heat and force.

2.2. Blending simulations

Once the intermittency factor on a surface is calculated, it is possible to blend a laminar and turbulent surface simulation file to assess the overall heat flux. However, when the boundary layer starts to transition, the global flow properties change and therefore the flow within the transition zone is different to a pure laminar regime. Particularly in laminarly separated zones, its extent might be drastically reduced within the transitional regime due to impact of turbulent features. Therefore, a methodology is setup which allows to blend a laminar and turbulent field simulation after a transition analysis (i.e., onset and extent) is performed. Afterwards, the BLITZ tool can be rerun on the blended simulation to improve the accuracy of the boundary layer transition point. The blending for any arbitrary variable

ϕ is applied in the complete computational domain using the intermittency γ with a relaxation factor α i.e.,

$$\phi_{new} = \alpha(\gamma\phi_{turb} + (1-\gamma)\phi_{lam}) + (1-\alpha)\phi_{old} \quad \text{Eq. 6}$$

For points at the surface, the intermittency is known directly. However, for points away from the surface in the field solution the intermittency cannot be algebraically determined. Therefore, the closest wall point is used to retrieve the intermittency value. Using the blended solution in an iterative approach allows converging to a more accurate transition onset and extent solution. Using the aforementioned monitoring methodology, it is now possible to assess the influence of transition on the heat flux and aerodynamic forces by combining a laminar and turbulent simulation.

2.3. Improved boundary layer edge detection

As discussed by Hoffmann et al. [3] a boundary layer edge detection has been developed based on the combination of different criteria. This edge detection has been improved to do an iterative boundary layer edge detection by Jacobs and Steelant [2]. These previous developments were made assuming a laminar boundary layer profile. However, as we are now shifting to blended simulations the edge detection should be properly working for both laminar, turbulent and blended simulations. During initial analysis it has been observed that the boundary layer edge is detected too close to the surface resulting in lower intermittency growth and further downstream transition location detection. To tackle this problem, several improvements to the existing model are discussed next.

A first improvement is made in the derivative criterion used in the voting algorithm. As discussed in [3] the derivative criterion is fulfilled when

$$\left|\frac{d^n u}{dy^n}\right| < \epsilon_n = 0.5(\epsilon_I + \epsilon_{II}) \quad \text{Eq. 7}$$

in which

$$\epsilon_I = \left|\frac{d^n u}{dy^n}\right|_{min} + \beta * \left(\left|\frac{d^n u}{dy^n}\right|_{max} - \left|\frac{d^n u}{dy^n}\right|_{min}\right) \quad \text{Eq. 8}$$

and

$$\epsilon_{II} = \alpha_n * \left|\frac{d^n u}{dy^n}\right|_{ref} \quad \text{Eq. 9}$$

in which $\left|\frac{d^n u}{dy^n}\right|_{ref}$ is the mean value of the nth $(n = 1{,}2)$ derivative at the different points along the wall normal profile where the derivative is below ϵ_I while $\alpha_1 = 3$ and $\alpha_2 = 2$. As for the turbulent boundary layer the derivative at the wall is significantly higher, Eq. 7 is triggered closer to the wall. To avoid this, the coefficient β is changed from 0.1 to 0.01 in the initial detection (where nearest neighbor interpolation is used iteratively) and from 0.03 to 0.005 for the final calculation (using linear interpolation). These changes are identical for both the first and second derivative criterion, respectively ϵ_1 and ϵ_2.

So far, the previous criteria are only enabled for the very first point along the wall normal where the specific criterion is triggered. Especially when using finely resolved boundary layers, this often results in different locations for the first and second derivative criterion (eq. 6). To improve this, a new combined criterion is added to the already existing criteria. This criterion is triggered at the first location along the wall normal where the ϵ-criterion (Eq. 7) is triggered for both the first and second derivative simultaneously, i.e.,

$$\left|\frac{du}{dy}\right| < \epsilon_1 \text{ and } \left|\frac{d^2 u}{dy^2}\right| < \epsilon_2 \quad \text{Eq. 10}$$

with ϵ_1 and ϵ_2 still defined as in Eq. 7.This methodology strengthens the previous two singular ϵ-criteria by adding an increased importance to the nearest point obtained from the combined ϵ-criterion. Obviously, the combined criterion is triggered only when the other two criteria (being second or first derivative criterion depending on the case) has already been satisfied.

A third and final improvement is made in the voting scheme for which the importance of the velocity criterion is increased with respect to the first and second derivative compared to the original formulation [3] and with the addition of the combined criterion. The coefficients are now as follows:

$$\begin{aligned} voting\ score = {} & 2.1 * (99\%\ velocity\ criterion) \\ & + 0.55(local\ max\ velocity\ criterion) + 1.65 * \left(\frac{du}{dy}\ criterion\right) \\ & + 1.65\left(\frac{d^2u}{dy^2}\ criterion\right) + 0.75 * \left(\frac{du}{dy}, \frac{d^2u}{dy^2}\ combined\ \ criterion\right) \end{aligned} \quad \text{Eq. 11}$$

Note that still local influence diffusion (LID) is used for all cases as was discussed by Hoffmann et al. [3]. LID is adding a diffusion term around the location i where the criterion is triggered. This is done by adding a term to the criterion at points $i \pm 1$. In this way the edge is more likely to be detected in regions where multiple criteria are triggered. Increasing the importance of the velocity criterion results in a better edge detection mainly when the ϵ-based criteria are triggered too low due to e.g. a very high wall derivative.

Due to the proposed changes the boundary layer edge is detected further away from the surface. However, to properly calculate the integrated values like displacement or momentum thickness, it is of major importance to not underestimate the boundary layer thickness. Therefore, an overprediction is less critical assuming a high enough resolution is present within the boundary layer.

3. Validation of implementation: T3A

To validate the developed methodology, a new analysis on the T3A flat plate reference case is performed. Therefore, both a laminar and a turbulent simulation are obtained and compared to experimental data. To assess the boundary layer transition the Mayle criterion [14] is used which is defined as

$$Re_{\theta,tr} = 420 * Tu_{\infty}^{-0.69} \quad \text{Eq. 12}$$

For the transition detection we are using the freestream turbulence level as perceived at the transition location of the T3A case, i.e. 2.197%. The skin friction evolution is shown in Fig. 1. Two blended simulations are present, one where only the surface files are blended (i.e. blending the skin friction coefficient) and one where the complete field is blended. A good agreement with the experimental data is obtained. However, the overshoot present in the experimental data cannot be reproduced due to the inherent limitations of the blending methodology.

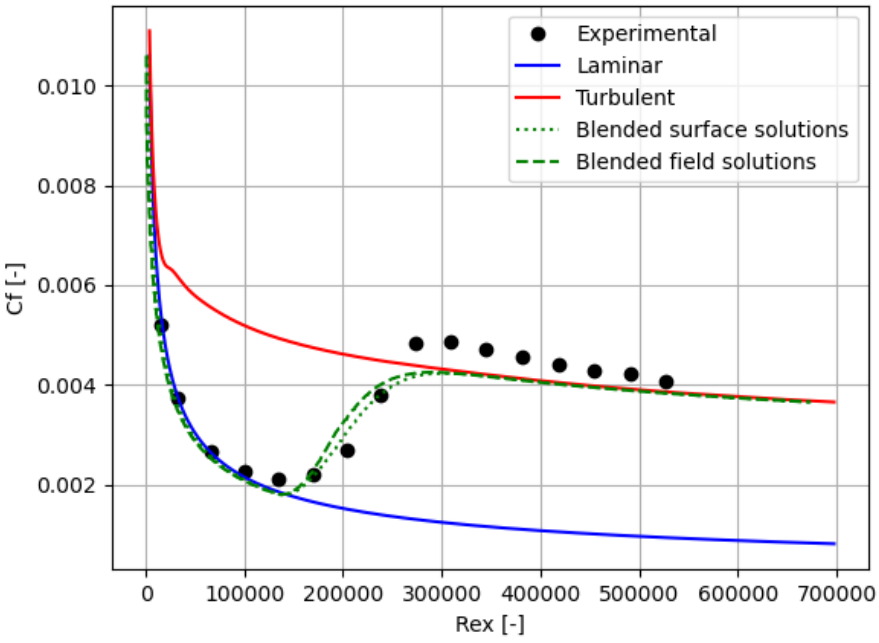

Fig. 1 Skin friction for the T3A reference case

4. HEXAFLY-INT experimental flight test vehicle analysis

A transition analysis along the trajectory of the experiment flight test vehicle (EFTV) is performed. The altitude, Mach number and angle of attack along the trajectory of the flight vehicle can be seen in Fig. 2, in which the dots mark the trajectory points at which simulations are performed. All simulations are performed using radiative equilibrium with a surface emissivity of 0.4.

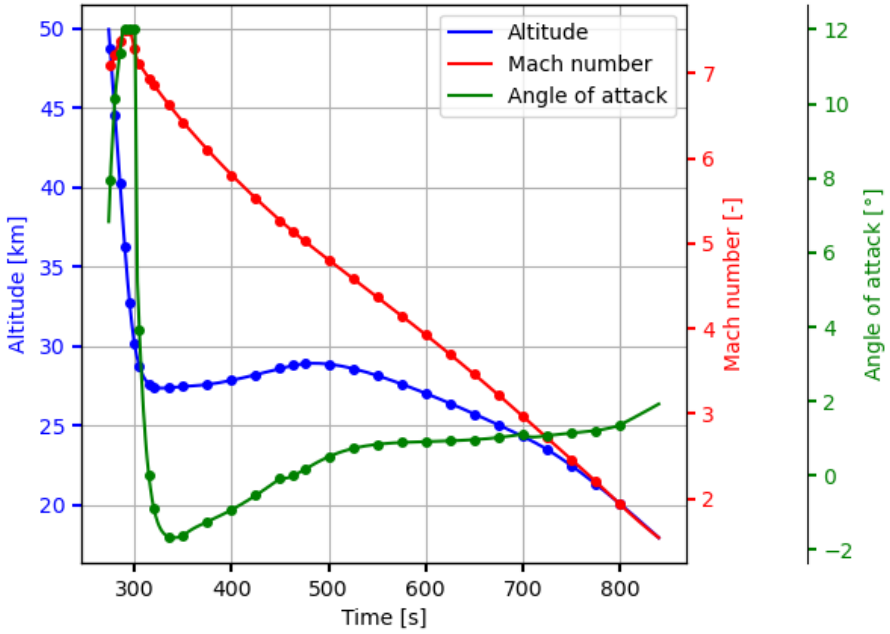

Fig. 2 Altitude, Mach number and angle of attack along the trajectory of the EFTV

4.1. Monitoring properties

To assess the correct implementation of the monitoring routine, the obtained integrated properties are compared to the values provided directly as outcome of the CFD code TAU of DLR for the simulation at T+314s. In Table 2 and Table 3, the results are compared for a laminar and a turbulent simulation, respectively. For the major components of the force good results are obtained. Only, for the smaller components of the viscous force, a relative (not absolute) difference is present with respect to the CFD value. The calculated heat load, which is either derived from conduction (Fourier law) or thermal radiation (Stefan-Boltzmann) for this validation, shows good agreement with the CFD solution.

Table 2. Validation of monitoring properties for the laminar solution

Integrated property	TAU code	BLITZ	Relative deviation
Pressure Force X [N]	636	636	0%
Viscous Force X [N]	103	104	0.96%
Pressure Force Y [N]	253	252	0.40%
Viscous Force Y [N]	-1.44	-1.54	6.49%[3]
Pressure Force Z [N]	2920	2919	0.03%
Viscous Force Z [N]	-8.36	-8.39	0.36%
Heat load: conduction [W]	67,561	65,529	3.1%
Heat load: radiation [W]	67,561	67,377	0.27%

[3] Note that even though the relative deviation is large, the absolute deviation is limited. Furthermore, this force will be cancelled out when a full-body is used instead of a half body for the simulation.

Table 3. Validation of monitoring properties for the turbulent solution

Integrated property	TAU code	BLITZ	Relative deviation
Pressure Force X [N]	642	642	0%
Viscous Force X [N]	264	266	0.76%
Pressure Force Y [N]	189	188	0.53%
Viscous Force Y [N]	4.1	3.9	4.88%[3]
Pressure Force Z [N]	2971	2971	0%
Viscous Force Z [N]	-19.3	-19.3	0%
Heat load: conduction [W]	145,268	138,818	4.6%
Heat load: radiation [W]	145,268	145,221	0.03%

The larger deviation in heat load for the conductive calculation compared to the radiative calculation shows that the deviation is caused by a discretization error during the derivative calculation. Note that the ratio between the laminar and turbulent heat flux differs very little: 0.465 for the TAU solution to 0.472 for the BLITZ simulation. Therefore, trends in change of heat flux calculated from the conduction are assumed to be correct, even though the absolute values might deviate slightly. Nevertheless, in the following results the radiative heat flux is used to ensure the best possible results.

4.2. Blending

Fig. 3 shows the heat load relative to the fully laminar and fully turbulent heat load for the simulation at T+314s. For lower relaxation factors the convergence takes longer, which is as expected. However, they are all converging to a similar value. This methodology allows to blend laminar and turbulent solutions and apply transition correlations on the blended solution. A major drawback of the current methodology is that it cannot predict the heat flux overshoot in the transitional regime or during a shock wave impingement since only a blending of the laminar and turbulent simulation is performed. For the simulations discussed in the remainder of this work a relaxation factor of 0.75 will be used.

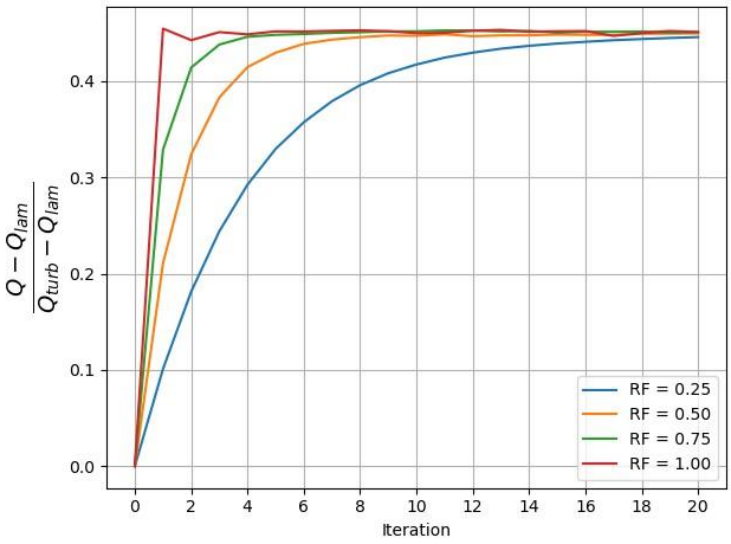

Fig. 3 Blended heat flux evolution for different relaxation factors

4.3. Transition location evolution

A first analysis is performed on the temporal boundary layer transition location based upon fully laminar solutions for the complete trajectory (i.e., from T+275s up to T+800s). As both laminar and turbulent simulations are available along the trajectory, a blended transitional analysis is constructed as well. For the transition onset, the Bowcutt [17] criterion is used:

$$\log\left(Re_{x,tr}\right) = 6.421 * \exp\left(1.209 \times 10^{-4}\, Ma_e^{2.641}\right) \quad \text{Eq. 13}$$

Fig. 4 shows the location of the most forward and most backward transitional point on the symmetry plane of the EFTV at different time steps for both a laminar and a blended transition analysis. It shows that the blending has only little influence on both the location of transition onset as well as the extent of the transition region. Initially at T+275s, no transition is happening, and the vehicle is fully laminar (Fig. 5). At T+290s (Fig. 6), the transition onset location starts to move forward up to T+300s (Fig. 7). Note that at this point the transition is only happening at the windward side. As the angle of attack decreases to zero degree at T+315s (Fig. 8), transition is also triggered on the leeward side. After T+315s the transition location is moving slowly backwards again up to T+500s (Fig. 9) due to the increase in altitude between those timesteps. Afterwards, it is again moving forwards until the end of the experiment at T+800s (Fig. 10).

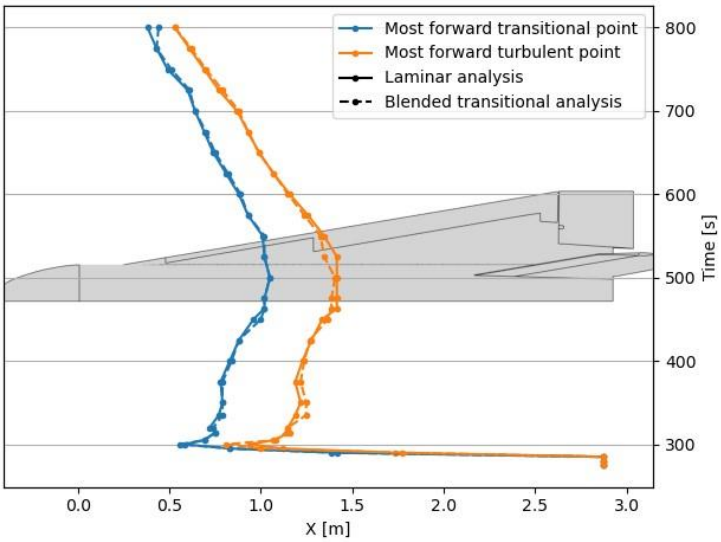

Fig. 4 Transition location on the symmetry plane of the EFTV

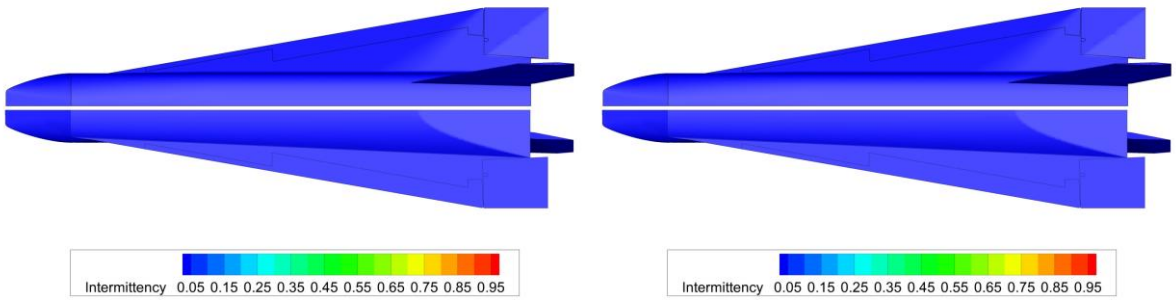

Fig. 5 T+275s - Mach 7.09 - Altitude 49km - AoA 7.94deg (left: laminar, right: blended transitional)

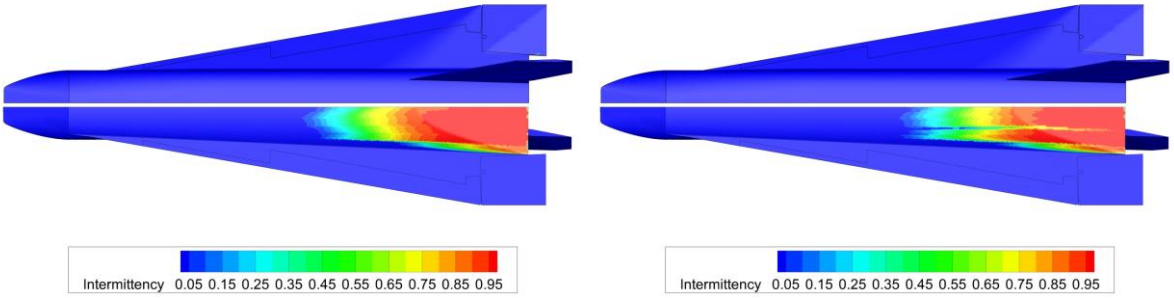

Fig. 6 T+290s - Mach 7.50 - Altitude 36km - AoA 12deg (left: laminar, right: blended transitional)

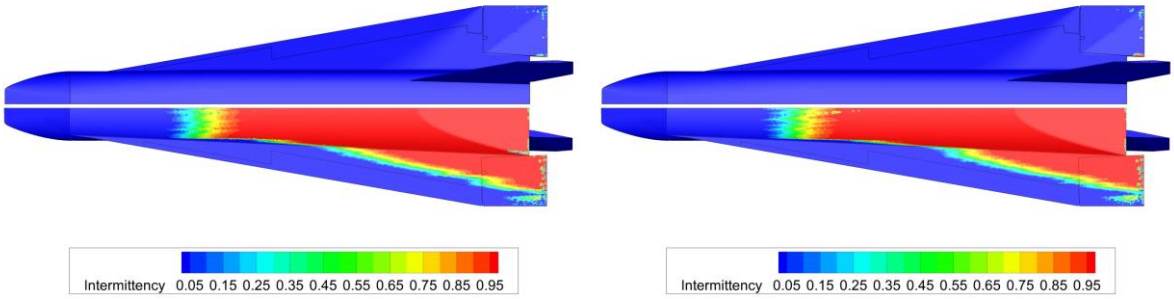

Fig. 7 T+300s - Mach 7.28 - Altitude 30km - AoA 12deg (left: laminar, right: blended transitional)

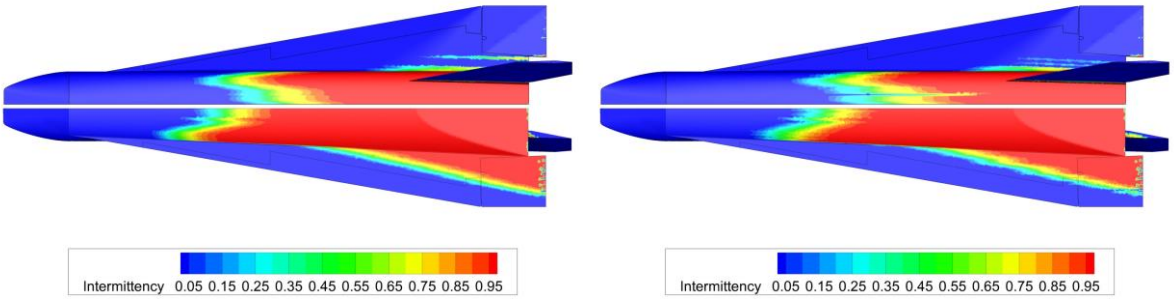

Fig. 8 T+315s - Mach 6.94 - Altitude 28km - AoA 0deg (left: laminar, right: blended transitional)

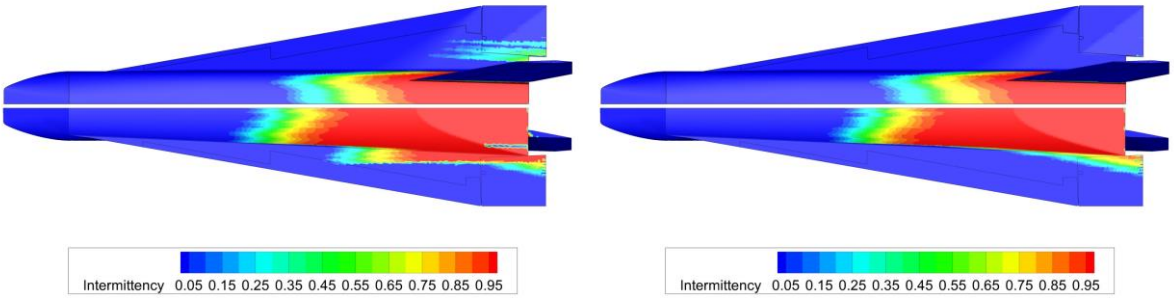

Fig. 9 T+500s - Mach 4.81 - Altitude 29km - AoA 0.51deg (left: laminar, right: blended transitional)

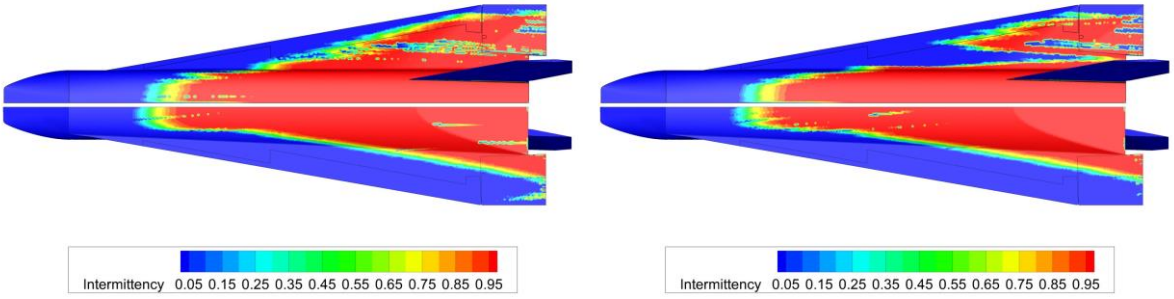

Fig. 10 T+800s - Mach 1.93 - Altitude 20km - AoA 1.37deg (left: laminar, right: blended transitional)

Fig. 11 shows the fraction of the time during the complete trajectory that a surface location is spent in the transitional regime. This is done for both the laminar and blended solution to further assess the impact on the intermittency growth. A difference is present, especially seen on the windward side of the wing. For the blended simulation, a narrow-closed region is in the transitional regime for more than 65% of the time, whilst this is only the case for some smaller spots on the laminar analysis of the vehicle. On the leeward side of the vehicle, the zone which is more than 10% of the time in transition is smaller on the wing for the blended analysis. Even though differences are present, in general a good agreement between the two types of simulations is present as expected. The main motivation for blending the simulations is to assess to overall heat load of the vehicle considering the change in boundary layer state. The region where transition occurs is relatively narrow. Due to heat flux overshoots experienced during boundary layer transition, additional care should be taken in this band during the design of the thermal protection system.

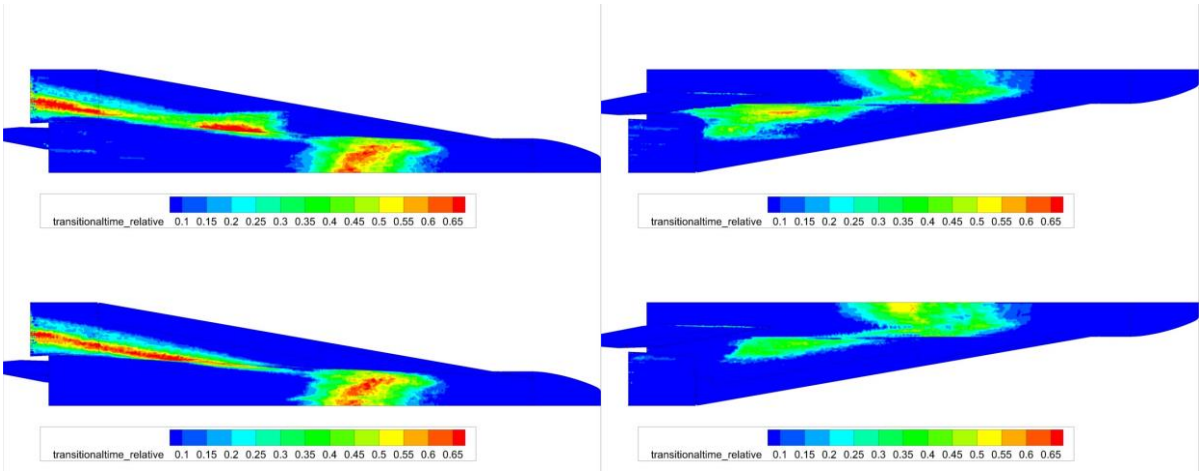

Fig. 11 Fraction of time in the transitional regime for the laminar (top) and blended (bottom) solutions for the windward (left) and leeward (right) side of the vehicle

4.4. Integrated heat load

During the design of the thermal protection system, it is useful to have an idea of the time integrated heat load coming into the vehicle. Fig. 12 shows the integrated heat load over the vehicle for the part of the trajectory for fully laminar, transitional and fully turbulent simulations. Note that we assume in this and the next sections that no roughness induced transition is taking place. As expected, the heat load of the vehicle is significantly higher for the blended simulations compared to the laminar ones due to the transition taking place. A difference is especially present on the body of the vehicle, whilst the wings are less influenced between laminar and blended solution. The opposite occurs if one compares laminar with pure turbulent. Hence tailoring of thermal protection systems would end up in complete wrong assessments if transition is not considered during the design process.

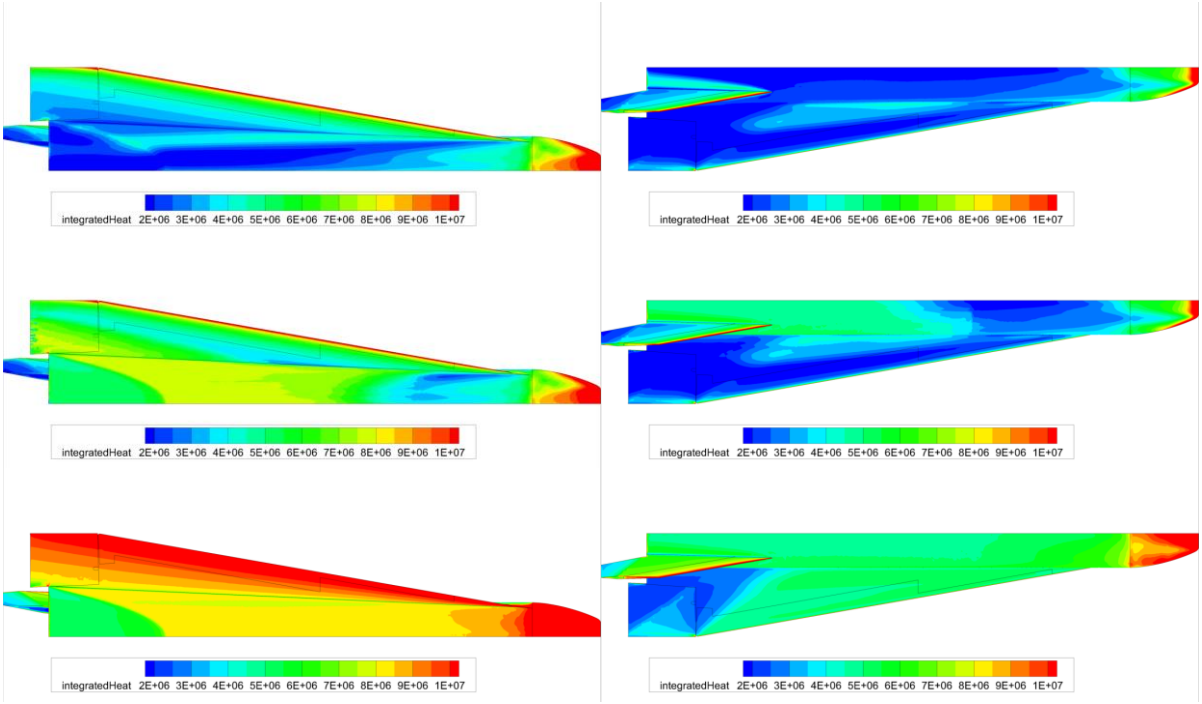

Fig. 12 Integrated heat load for the EFTV using laminar (top), blended (middle) and turbulent (bottom) solutions for the windward (left) and leeward (right) side of the vehicle

To assess the impact of applying a proper blending methodology, a comparison is made between the blended, the fully laminar and the fully turbulent case. The surface averaged heat flux and the surface integrated accumulated heat load are shown in Fig. 13 for the total vehicle as well as for the leeward and windward side separately. Indeed, a significant difference is present with respect to the fully laminar or turbulent solutions for the complete vehicle but also for the leeward and the windward side separately. Therefore, designing the thermal protection system purely on the turbulent heat load would overdimension the thermal protection system. The peak in the total heat flux around T+300s is explained by the high angle of attack, high Mach number and low altitude for this simulation. After T+300s, the angle of attack starts to decrease rapidly.

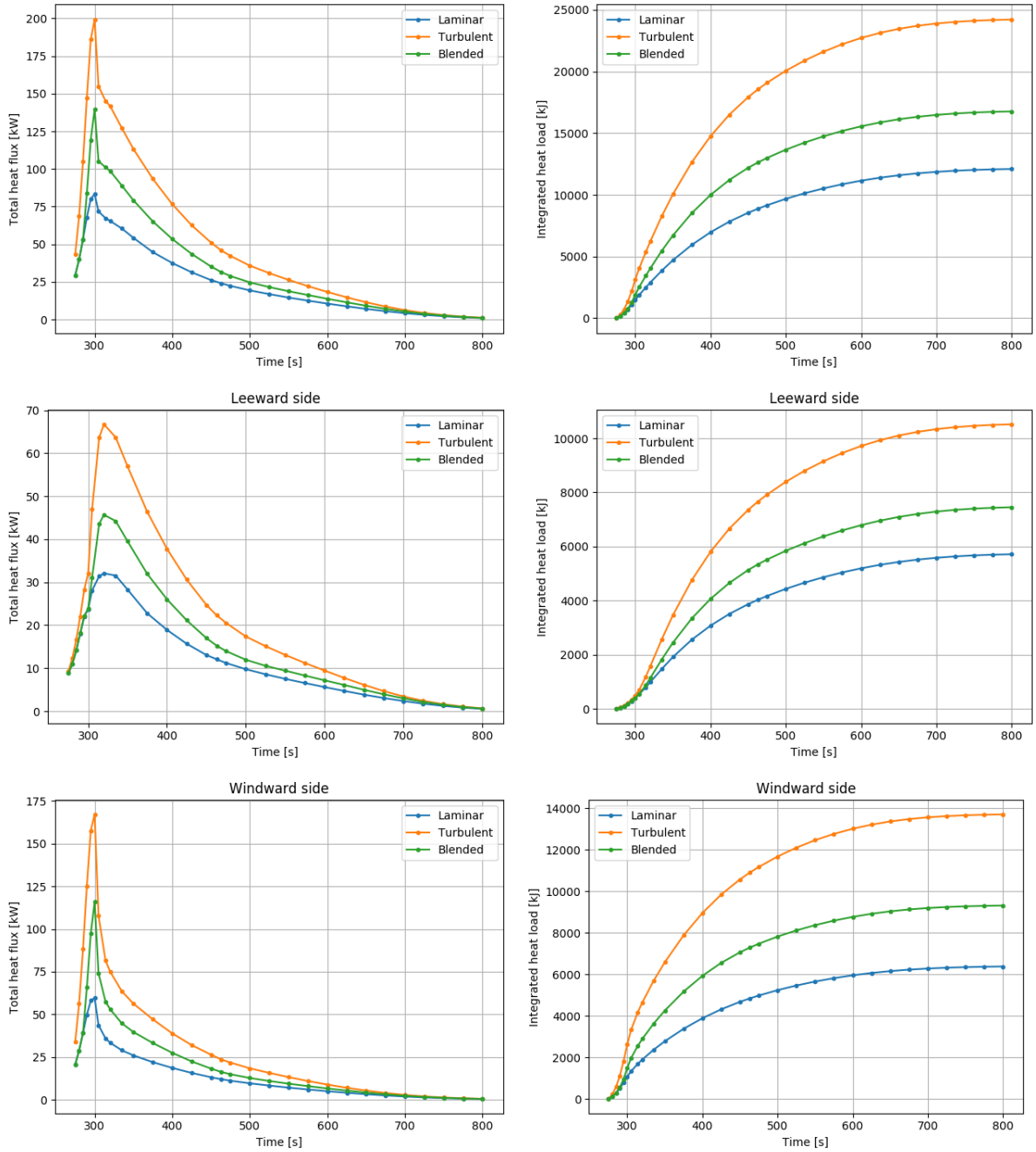

Fig. 13 Vehicle surface integrated heat flux (left) and integrated heat load (right) for the complete vehicle (top), leeward side of the vehicle (middle) and windward side of the vehicle (bottom)

Fig. 14 shows the relative weight of the turbulent heat flux and the ratio between the blended heat flux and the turbulent heat flux for the total integrated heat load. The relative turbulent weight is defined as

$$relative\ turbulent\ weight = \frac{Q_{blended} - Q_{laminar}}{Q_{turbulent} - Q_{laminar}} \qquad \text{Eq. 14}$$

Fig. 14 shows that the ratio for the total integrated heat load goes down to about 0.7 for the total vehicle. This means that the total heat load is 30% lower than the purely turbulent integrated heat load.

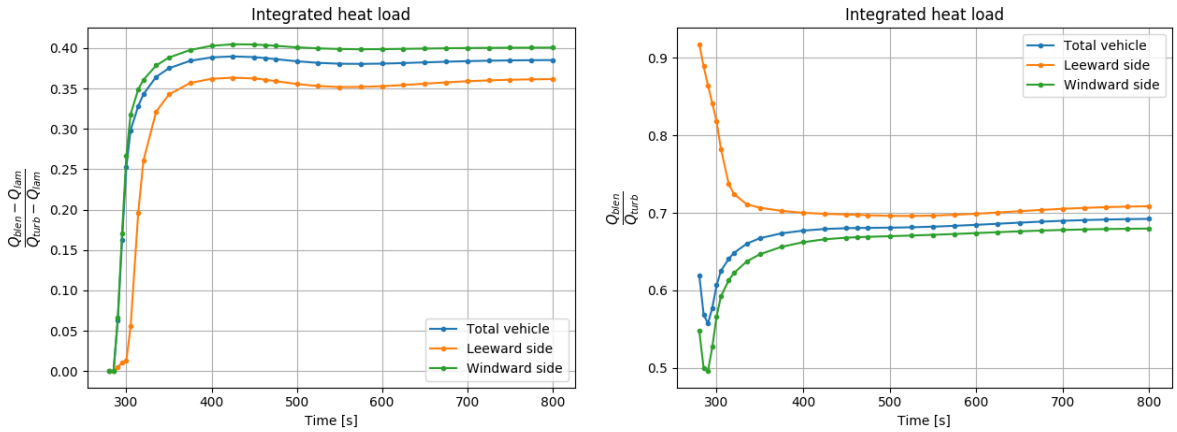

Fig. 14 Relative weight (left) and blended to turbulent ratio (right) for the integrated heat load

A local distribution of the relative turbulent weight and the blended to turbulent ratio for the accumulated heat load can be seen in Fig. 15. In the front part of the vehicle, the heat load is locally up to 70% below the turbulent value. However, near the back, the values are closer to the turbulent heat load since the flow is turbulent at that location for the majority of the trajectory.

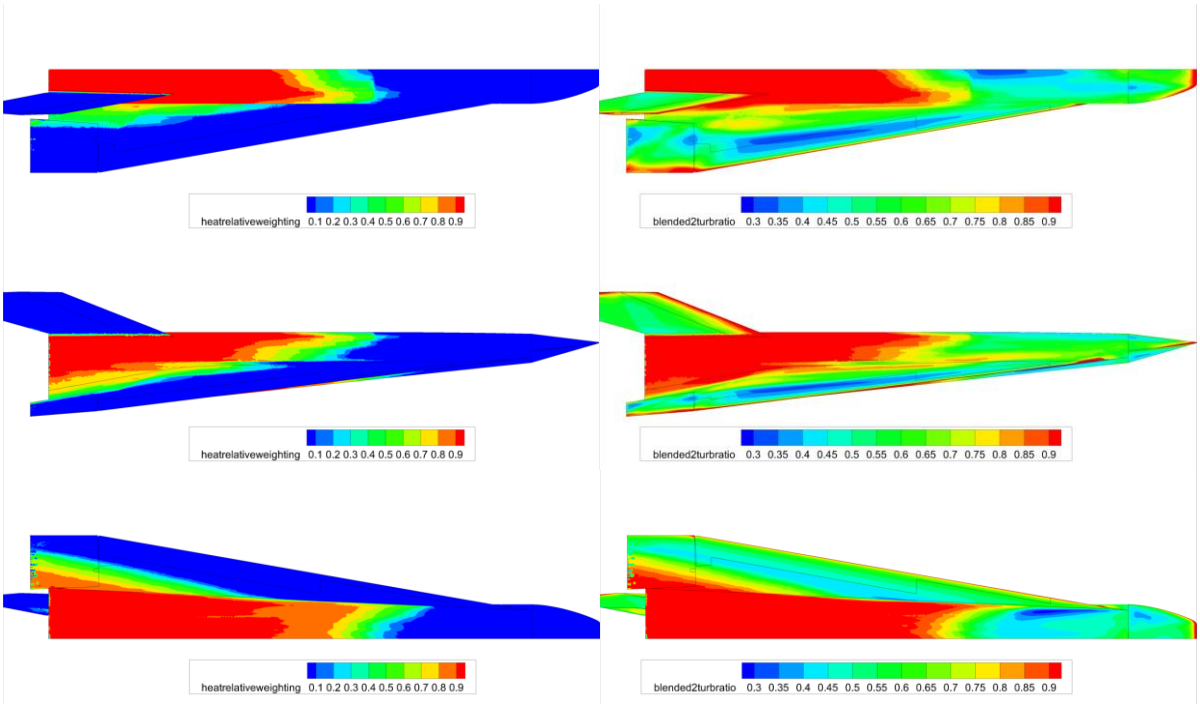

Fig. 15 Local distribution of the relative turbulent weight (left) and the blended to turbulent ratio (right) for the accumulated heat load in top, side and bottom view

4.5. Aerodynamic forces

Another parameter to consider is the aerodynamic force, which is important to calculate the flight path of the vehicle. Fig. 16 shows the viscous, pressure and total force in the nose-to-tail-direction for the laminar, turbulent and blended simulations. The peak at T+300s for all forces is again explained by the large angle of attack, high Mach number and the low altitude at that point of the trajectory. As mentioned before, the angle of attack starts to decrease after this timestep. The forces for the blended simulation are significantly lower for the viscous and the total force than the turbulent values, but not for the pressure force. This is confirmed by Fig. 17, which shows the blended to turbulent ratio for the

different forces. The pressure force is only slightly influenced by the blending as expected whereas the viscous force is about 40% lower compared to the purely turbulent simulations. This results in a total force which is around 10% lower compared to a fully turbulent analysis at high Mach numbers, showing the importance of a transitional analysis. A fully laminar vehicle can result in forces up to 20% lower than a fully turbulent vehicle.

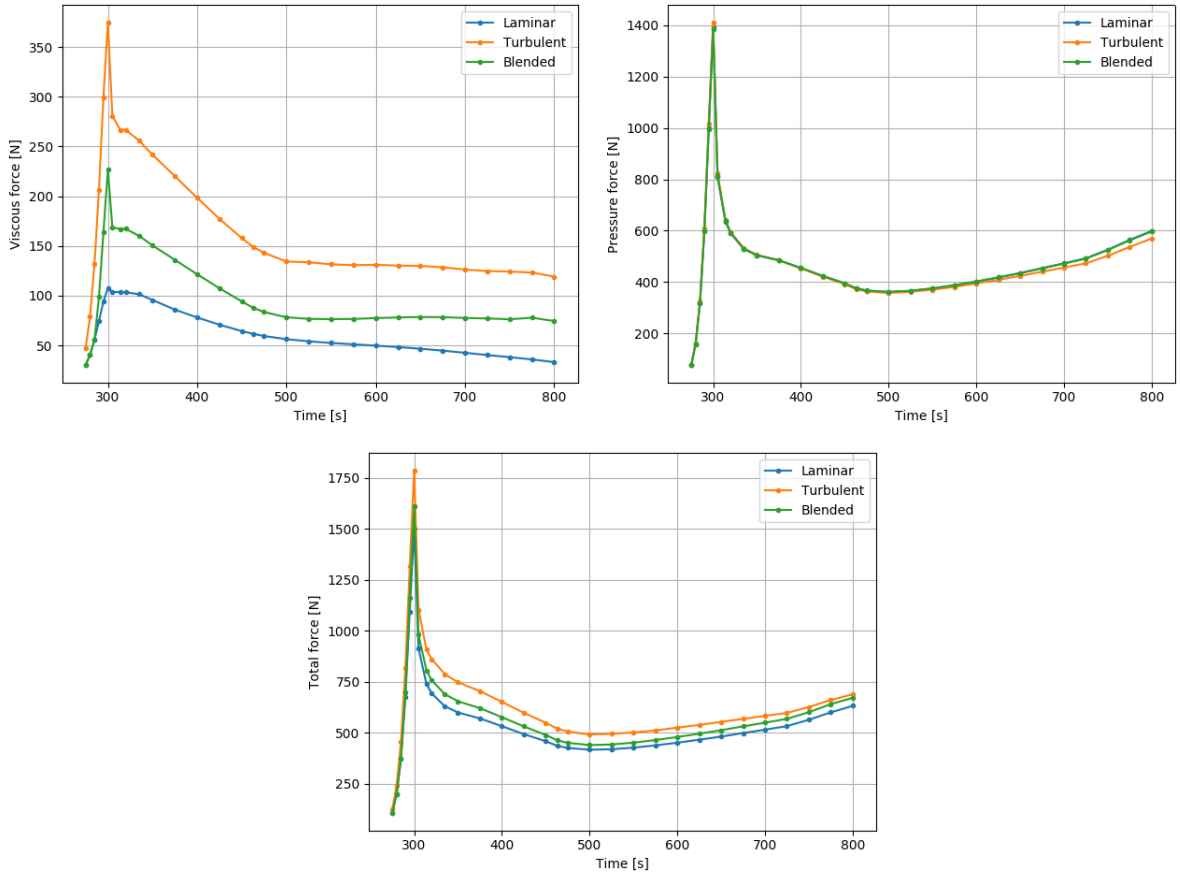

Fig. 16 Viscous (top left), pressure (top right) and total (bottom) force in the vehicle the nose-to-tail direction

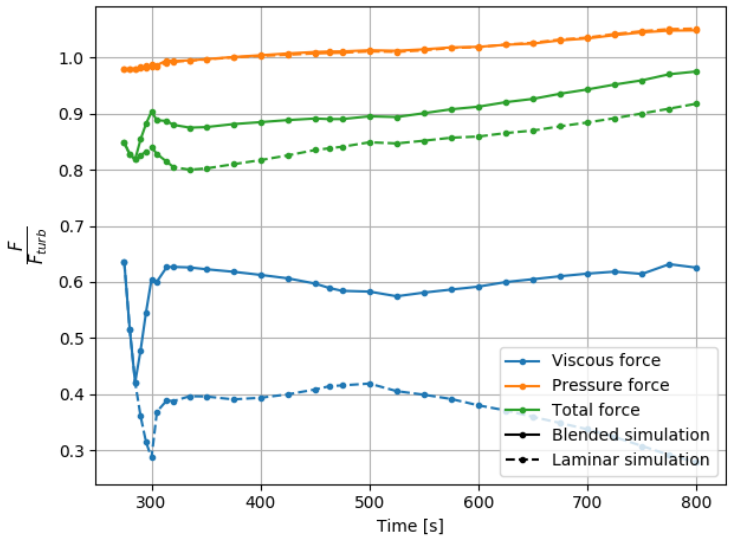

Fig. 17 Blended and laminar force relative to turbulent force for the viscous, pressure and total force in the vehicle the nose-to-tail direction

5. Effect on vehicle sizing

In this section we discuss the influence of the reduction of heat and drag on the vehicle weight and fuel requirements. As no mass breakdown is made available for the HXI EFTV, an analysis is performed on the LAPCAT vehicle, which is very similar to the EFTV in shape and trajectory. The mass breakdown of this vehicle is discussed in [20]. The complexity of the analysis is gradually increased in different steps as discussed in the next paragraphs. An overview of the mass of the different components as well as the reduction for different approaches discussed next is shown in Table 4. We use a reduction of 10% in aerodynamic forces and 30% in heat load. It is important to mention that these properties are determined on a scaled version of the vehicle and transition might happen more towards the front on a full-scale vehicle.

To assess the performance of the vehicle, the Breguet range is kept constant. Furthermore, we assume the same payload (60,000kg), same flight speed and same I_{sp}. Using these assumptions results in the following equality.

$$R = V\left(\frac{L}{D}\right)_{turb} I_{sp} \ln\left(\frac{W_{to}}{W_{la}}\right)_{turb} = V\left(\frac{L}{D}\right)_{trans} I_{sp} \ln\left(\frac{W_{to}}{W_{la}}\right)_{trans} \quad \text{Eq. 15}$$

Since we know that the drag is reduced with 10%, it is possible to find the initial over final weight ratio for a fully turbulent and a transitional vehicle.

$$\left(\frac{W_{to}}{W_{la}}\right)_{trans} = \left(\frac{W_{to}}{W_{la}}\right)_{turb}^{0.9} \quad \text{Eq. 16}$$

A first approach only considers the reduction in fuel due to this equation and assumes that the vehicle is built such that no modifications can be made. Doing this results in a gross take-off weight (GTOW) reduction of 6% and a fuel reduction of 13%. It is clear that this has a significant impact.

Secondly, as the heat is also reduced by 30% it could be assumed that the mass of the thermal protection system (TPS) can be reduced by 30% as well. Combining this new TPS weight with Eq. 16 results in a GTOW decrease of 7% and a fuel reduction of 14%. The small difference with respect to the previous values is explained due to the limited contribution of the TPS to the total mass of the vehicle.

As now the GTOW is reduced, the structure needs to carry less weight. It is assumed that to design the vehicle the weight of the body, wing and landing gear is proportional to the GTOW. Since a reduction in structural weight is also influencing the GTOW, an iterative approach is used. First the weight of the TPS is reduced with 30%. Then the structural weight is recalculated such that it is proportional to the current GTOW. Based on this new landing mass, the required fuel is calculated using Eq. 16. This changes the GTOW again and thus is the structural weight scaled again and the fuel recalculated. This is repeated 10 times at which time the obtained mass is nicely converged as shown in Fig. 18 (left). In this case the fuel mass is reduced with 17% and the GTOW, and the weight of the structural elements is reduced with 11%. This is again showing a significant impact on the total weight of the vehicle.

A final approach focuses on the propulsion system as well. Since the drag is reduced with 10%, the propulsion system can be reduced in size. We assume for this calculation that the weight of the propulsion system is also reduced with 10%. Reducing the propulsion system mass with 10% and the TPS with 30% and performing the same steps as discussed for the previous approach results in the mass convergence in Fig. 18 (right). In this case the total fuel mass required to maintain the same range is 21% below the fully turbulent analysis. Furthermore, the GTOW and weight of the structural elements is reduced with 15%.

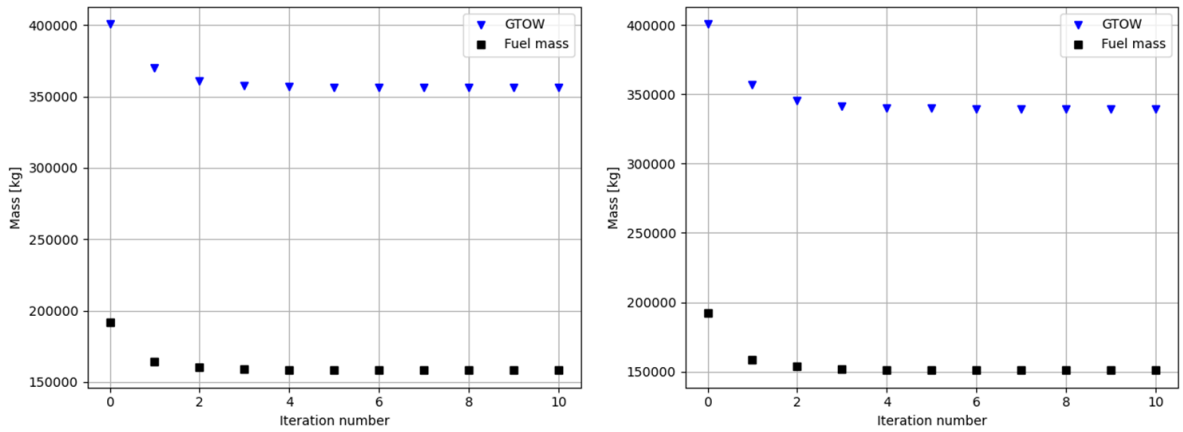

Fig. 18 Mass evolution during the iterative approach without (left) and with (right) scaling of propulsion system

Table 4. Weight reduction for different assumptions

	Original weight [kg] [20]	**Fuel**	**Fuel + TPS**	**Fuel + TPS + Structure**	**Fuel + TPS + Structure + Propulsion**
Body	48,589	=	=	-11%	-15%
Wing	16,973	=	=	-11%	-15%
TPS	7819	=	-30%	-30%	-30%
Gear	8641	=	=	-11%	-15%
Propulsion	61,320	=	=	=	-10%
Control	1992	=	=	=	=
Power supply	3180	=	=	=	=
Payload	60,000	=	=	=	=
Fuel	192,000	-13%	-14%	-17%	-21%
GTOW	400,514	-6%	-7%	-11%	-15%
Landing Weight	208,514	=	-1%	-5%	-9%
Vehicle Dry Weight	148,514	=	-2%	-7%	-13%

It is clear that the mass is significantly impacted by the use of a transitional rather than a fully turbulent analysis. If the vehicle is not changed, the fuel mass can be reduced with 13%. When all the assumptions are applied, i.e., fuel reduction, TPS and propulsion system mass reduction and structural mass reduction, a fuel reduction of 21% is obtained. Additionally, a GTOW reduction of 15% is present in this last case. The weight of the empty vehicle, not including fuel or payload, is reduced with 13%. If we assume that the cost of an aircraft is proportional to its weight, this results in a reduction of 13% as well.

6. Conclusion

This paper presents the first results of the blending methodology between laminar and turbulent simulations to reconstruct a transitional flow. We presented a first trajectory analysis of both laminar and blended simulations for the HEXAFLY-INT Experimental Flight Test Vehicle. The presented trajectory analysis shows the evolution of the boundary layer state, the integrated heat load and the aerodynamic forces exerted on the vehicle. It has been shown that a difference of 10% in the

aerodynamic force is observed between the blended and turbulent simulations, which is of major importance for the trajectory determination. It was shown that the integrated heat load can be 30% lower over the complete surface and 70% lower locally for the blended simulations. Finally, different critical protuberances along the surface of the flight vehicle are calculated to guarantee that no transition is triggered at that location throughout the complete trajectory. Both the integrated heat load as well as the critical surface parameters allow to properly design the surface and thermal protection system and are extremely useful for designers of hypersonic vehicles. We have shown that taking transitional properties rather than fully turbulent values, can result in a fuel saving of 13% if the vehicle is used as is. If the vehicle would have been designed using the transitional model, a reduction with 21% on the fuel mass and 15% on the GTOW could be achieved. In this case the mass of the empty vehicle, which can be assumed to be proportional to the cost of the aircraft, goes down with 13%. This proves again the importance of applying the mentioned transitional models in an early stage of the design.

References

[1] N. Sandham and J. Van den Eynde, "Outcome of high-speed boundary layer transition workshop at HiSST 2022," *CEAS Space Journal*, May 2023, doi: 10.1007/s12567-023-00503-1.

[2] F. Jacobs and J. Steelant, "Temporal Evolution of Transition Onset along Trajectories of Generic Flight Vehicles," in *Aerospace Europe Conference*, EUCASS-CEAS, 2023. doi: http://dx.doi.org/10.13009/EUCASS2023-315.

[3] J. P. Hoffmann, J. Van den Eynde, and J. Steelant, "An analysis tool for boundary layer and correlation-based transition onset assessment on generic geometries," *CEAS Space Journal*, Jul. 2023, doi: 10.1007/s12567-023-00507-x.

[4] M. Karsch, J. Van den Eynde, and J. Steelant, "Linearly combined transition model based on empirical spot growth correlations," *CEAS Space Journal*, May 2023, doi: 10.1007/s12567-023-00499-8.

[5] J. Steelant *et al.*, "Flight Testing Designs in HEXAFLY-INT for High-Speed Transportation," in *1st International Conference on High-Speed Vehicle Science and Technology (HiSST)*, Moscow, Russia, Nov. 2018.

[6] S. Di Benedetto *et al.*, "The high-speed experimental flight test vehicle of HEXAFLY-INT: a multidisciplinary design," *CEAS Space Journal*, vol. 13, no. 2, pp. 291–316, Apr. 2021, doi: 10.1007/s12567-020-00341-5.

[7] J. Steelant *et al.*, "Boundary Layer Transition Assessment on a Slender High-Speed Vehicle," in *21st AIAA International Space Planes and Hypersonics Technologies Conference*, Reston, Virginia: American Institute of Aeronautics and Astronautics, Mar. 2017, p. 140180. doi: 10.2514/6.2017-2133.

[8] S. Dhawan and R. Narasimha, "Some properties of boundary layer flow during the transition from laminar to turbulent motion," *J Fluid Mech*, vol. 3, no. 4, pp. 418–436, Jan. 1958, doi: 10.1017/S0022112058000094.

[9] J. Steelant and E. Dick, "Modelling of bypass transition with conditioned Navier-Stokes equations coupled to an intermittency transport equation," *Int J Numer Methods Fluids*, vol. 23, no. 3, pp. 193–220, 1996, doi: 10.1002/(SICI)1097-0363(19960815)23:3<193::AID-FLD415>3.0.CO;2-2.

[10] J. Steelant and E. Dick, "Modeling of Laminar-Turbulent Transition for High Freestream Turbulence," *J Fluids Eng*, vol. 123, no. 1, pp. 22–30, Mar. 2001, doi: 10.1115/1.1340623.

[11] J. Steelant and E. Dick, "Prediction of By-Pass Transition by Means of a Turbulence Weighting Factor: Part II — Application on Turbine Cascades," in *Volume 3: Heat Transfer; Electric Power; Industrial and Cogeneration*, American Society of Mechanical Engineers, Jun. 1999. doi: 10.1115/99-GT-030.

[12] J. Steelant and E. Dick, "Prediction of By-Pass Transition by Means of a Turbulence Weighting Factor: Part I — Theory and Validation," in *Volume 3: Heat Transfer; Electric Power; Industrial and Cogeneration*, American Society of Mechanical Engineers, Jun. 1999. doi: 10.1115/99-GT-029.

[13] A. Syrakos, S. Varchanis, Y. Dimakopoulos, A. Goulas, and J. Tsamopoulos, "A critical analysis of some popular methods for the discretisation of the gradient operator in finite volume methods," *Physics of Fluids*, vol. 29, no. 12, Dec. 2017, doi: 10.1063/1.4997682.

[14] R. E. Mayle, "The Role of Laminar-Turbulent Transition in Gas Turbine Engines," in *Volume 5: Manufacturing Materials and Metallurgy; Ceramics; Structures and Dynamics; Controls, Diagnostics and Instrumentation; Education; IGTI Scholar Award; General*, American Society of Mechanical Engineers, Jun. 1991. doi: 10.1115/91-GT-261.
[15] F. White, *Viscous Fluid Flow*, 2nd ed. McGraw-Hill Professional, 1991.
[16] H. Schlichting and K. Gersten, *Boundary-Layer Theory*. Berlin, Heidelberg: Springer Berlin Heidelberg, 2017. doi: 10.1007/978-3-662-52919-5.
[17] K. G. Bowcutt, J. D. Anderson, and D. Capriotti, "Viscous optimized hypersonic waveriders," in *25th AIAA Aerospace Sciences Meeting*, Reston, Virigina: American Institute of Aeronautics and Astronautics, Mar. 1987. doi: 10.2514/6.1987-272.
[18] S. Berry and H. Hamilton, "Discrete Roughness Effects on Shuttle Orbiter at Mach 6," in *32nd AIAA Fluid Dynamics Conference and Exhibit*, Reston, Virigina: American Institute of Aeronautics and Astronautics, Jun. 2002. doi: 10.2514/6.2002-2744.
[19] D. C. Reda, "Correlation of Nosetip Boundary-Layer Transition Data Measured in Ballistics-Range Experiments," *AIAA Journal*, vol. 19, no. 3, pp. 329–339, Mar. 1981, doi: 10.2514/3.50952.
[20] J. Steelant and M. van Duijn, "Structural Analysis of the LAPCAT-MR2 Waverider Based Vehicle," in *17th AIAA International Space Planes and Hypersonic Systems and Technologies Conference*, Reston, Virigina: American Institute of Aeronautics and Astronautics, Apr. 2011. doi: 10.2514/6.2011-2336.